Nondestructive Picosecond Ultrasonic Probing of Intralayer and van der Waals Interlayer Bonding in α- and β-In$_2$Se$_3$

Wenjing Yan,* Andrey V. Akimov,* Joseph A. Page, Mark T. Greenaway, Alexander G. Balanov, Amalia Patanè, and Anthony J. Kent

The interplay between the strong intralayer covalent-ionic bonds and the weak interlayer van der Waals (vdW) forces between the neighboring layers of vdW crystals gives rise to unique physical and chemical properties. Here, the intralayer and interlayer bondings in α and β polytypes of In$_2$Se$_3$ are studied, a vdW material with potential applications in advanced electronic and optical devices. Picosecond ultrasonic experiments are conducted to probe the sound velocity in the direction perpendicular to the vdW layers. The measured sound velocities are different in α- and β-In$_2$Se$_3$, suggesting a significant difference in their elastic properties. Density functional theory and an effective spring model are used to calculate the elastic stiffness of the layer and vdW gap in α- and β-In$_2$Se$_3$. The calculated elastic moduli show good agreement with experimental values and reveal the dominant contribution of interlayer atomic bonding to the different elastic properties of the two polytypes. The findings show the power of picosecond ultrasonics for probing the fundamental elastic properties of vdW materials. The data and analysis also provide a reliable description of the intra- and interlayer forces in complex crystal structures, such as the polytype phases of In$_2$Se$_3$.

1. Introduction

2D van der Waals materials (2D-vdW), such as graphene, MoS$_2$ and similar, are typically described as strong covalently/ionically bonded layered structures that are held together by weak vdW forces.[1,2] The utterly different nature and coexistence of these strong and weak forces allow the exfoliation and isolation of perfect single layered materials. Investigations of these types of materials have led to the discovery of a wide range of classical

and quantum phenomena such as capillary condensation,[3] the quantum anomalous Hall effect,[4] superconductivity, and carrier correlations.[5] However, despite this intensive investigation of vdW materials, there are only very few experimental techniques to measure nondestructively the strength of atomic bonds and vdW forces. The results of these experimental investigations reveal a great degree of discrepancy.[6–10] Also, calculations of the structural properties of vdW materials by density functional theory (DFT) are limited since the vdW forces can only be included by approximate methods, and more accurate quantum Monte Carlo-based calculations are extremely computationally costly.[11] The lack of understanding of these forces is becoming a bottleneck for the study and practical applications of functional systems. Detailed understanding both experimentally and theoretically in this area will permit important insight into the physical origin of the measured properties of materials and predict the properties of new polytype phases and heterostructures.

Here, we demonstrate an experimental technique, which can be used to measure the elastic properties of 2D-vdW materials. We consider the 2D-vdW material In$_2$Se$_3$, which can exist in several polytypes, α, β, β', γ and δ, each with a different crystalline structure that develops under different growth conditions.[12,13] This material demonstrates outstanding electronic properties, promising for a range of technological applications including solar cells,[14,15] photodiodes,[16] ferroelectric field-effect transistors,[17] and nonvolatile memory elements.[18] Of particular interest are α- and β-In$_2$Se$_3$. The α-phase is ferroelectric with different ferroelectric properties for hexagonal (2H) and rhombohedral (3R) structures with AB and ABC stacking of the individual quintuple layer, respectively.[17–25] On the other hand, β-In$_2$Se$_3$ (3R) is not ferroelectric and can emerge under thermal annealing of α-In$_2$Se$_3$.[26,27] Furthermore, superconductivity was reported in β-In$_2$Se$_3$ under high pressure due to phonon softening.[28]

A promising experimental approach to reveal the origin of the differences between the polytypes and the effect on the technologically and fundamentally important properties of In$_2$Se$_3$ is to study their dynamical elasticity. Such a study would provide information about intralayer and vdW atomic bonding, which govern the fundamental phonon transport properties, electron–phonon interaction, phase transition, and the mechanical exfoliation of vdW crystals. In this work, we study experimentally

W. Yan, A. V. Akimov, A. Patanè, A. J. Kent
School of Physics and Astronomy
University of Nottingham
Nottingham NG7 2RD, UK
E-mail: wenjing.yan@nottingham.ac.uk; andrey.akimov@nottingham.ac.uk
J. A. Page, M. T. Greenaway, A. G. Balanov
Department of Physics
Loughborough University
Loughborough LE11 3TU, UK

The ORCID identification number(s) for the author(s) of this article can be found under https://doi.org/10.1002/adfm.202106206.

and theoretically the dynamical elasticity of α- and β-In$_2$Se$_3$. We use the picosecond ultrasonic (PU) technique[29,30] to measure the sound velocity in flakes with thicknesses in the range $d \approx 30$–760 nm and observe a surprisingly big difference in the sound velocity between the two polytypes. The latter suggests a difference in the elastic properties of these polytypes despite their similar layer thickness and width of their vdW gaps. To provide insight into this finding, we performed DFT calculations, which show that different sound velocities arise from the variation in vdW forces due to different stacking sequences and crystal symmetry. The intralayer atomic bonding, although also different, has a weaker impact on the net elasticity compared to the vdW force. Our measurements provide an efficient and accurate way to determine the mechanical properties of vdW crystals. Hence, they can serve as a powerful tool for providing insight into the nature of interlayer vdW forces, which will inform the modeling and design of vdW heterostructures and devices.

2. Results and Discussion

2.1. In$_2$Se$_3$ Samples

Figure 1a shows the crystal structures of α-In$_2$Se$_3$ and β-In$_2$Se$_3$. In both polytypes, each quintuple layer consists of five atomic layers that are covalently bonded and sandwiched between two vdW gaps. The thickness of the α-In$_2$Se$_3$ and β-In$_2$Se$_3$ quintuple layer varies between 0.9 and 1 nm, with ≈30% of the thickness

corresponding to the vdW gap, as determined by X-ray and electron microscopy.[20,31] The stacking polymorph of studied α-In$_2$Se$_3$ is hexagonal (2H, space group P6$_3$mc) with two quintuple layers per unit cell; β-In$_2$Se$_3$ is instead rhombohedral (3R, space group $R\bar{3}m$) with three quintuple layers per unit cell. Flakes of α- and β- In$_2$Se$_3$ were mechanically exfoliated from bulk crystals purchased from HQ Graphene and dry transferred onto sapphire substrates. The thickness of the flakes was measured by atomic force microscopy (AFM) and ranges from $d \approx 7$ to 760 nm. The phases of In$_2$Se$_3$ can be easily distinguished by Raman spectroscopy measurements (Figure 1b). Exfoliated flakes show distinct Raman peaks at $A_1 = 104$ cm^{-1}, $E_g = 182$ cm^{-1}, $A_1 = 205$ cm^{-1} for α-In$_2$Se$_3$, and $A_1 = 110$ cm^{-1}, $E_g = 175$ cm^{-1}, $A_1 = 206$ cm^{-1} for β-In$_2$Se$_3$. A comparison of the broadening of the Raman lines in α-In$_2$Se$_3$ and β-In$_2$Se$_3$ suggests that the β-phase is more defective: the full width at half maximum (FWHM) of the A_1 peak in the α-phase is 2.8 cm^{-1}, smaller than for the β-phase (FWHM of 17.6 cm^{-1}). We do not observe the coexistence of different phases and, if any, the fraction of a different polytype within the laser spot should be less than 1%. We have conducted PU experiments on more than 30 flakes of α-In$_2$Se$_3$ and β-In$_2$Se$_3$.

2.2. Experiment

Figure 1c,d shows the schematic of the pump-probe (PU) experiments for measuring the velocity s of longitudinal phonons with wavevector perpendicular to the vdW layer plane
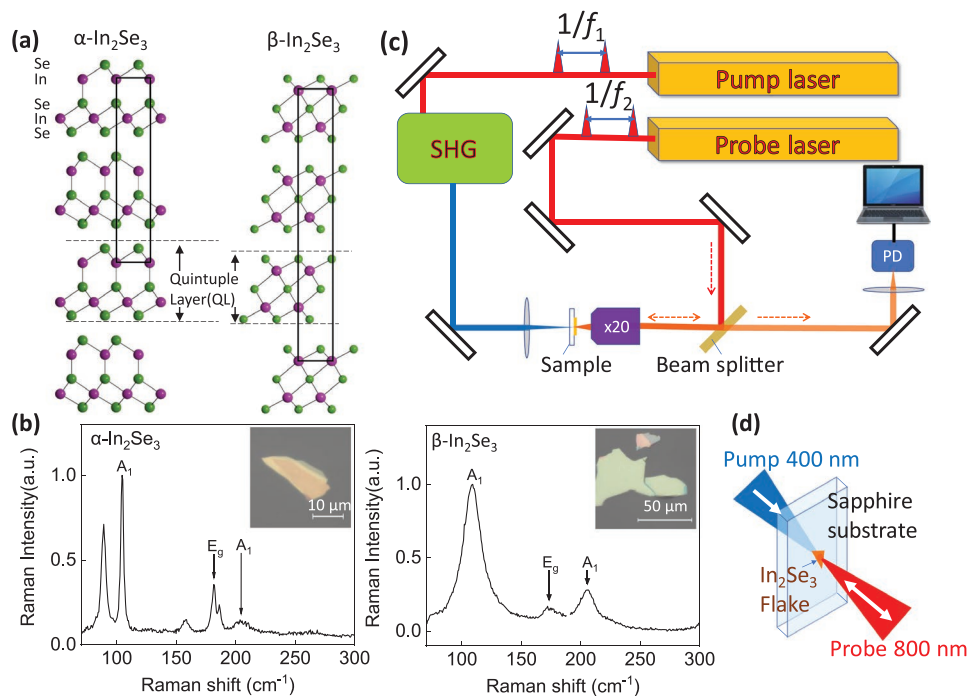

Figure 1. Samples and experimental setup. a) Crystal structure of α- and β-In$_2$Se$_3$.[20,31] The solid boxes mark the unit cells of α- In$_2$Se$_3$ (2H) and β-In$_2$Se$_3$ (3R). b) Raman spectra for α- and β-In$_2$Se$_3$ flakes; insets—optical images of the flakes. c) Schematic diagram of the pump-probe setup for measuring the sound velocity: PD—photodetector; SHG—second harmonic generator; f_1 and f_2 are repetition rates of pulses from pump and probe lasers, respectively. Here, f_1, $f_2 \approx 80$ MHz and a small difference $f_1 - f_2 = 800$ Hz results in a slow temporal scanning of the probe pulses relative to the pump pulses, providing a temporal resolution ≈1 ps. The dotted arrows show the direction of light. d) The zoomed fragment of the sample space in the PU experiments with 400 nm pump and 800 nm probe.
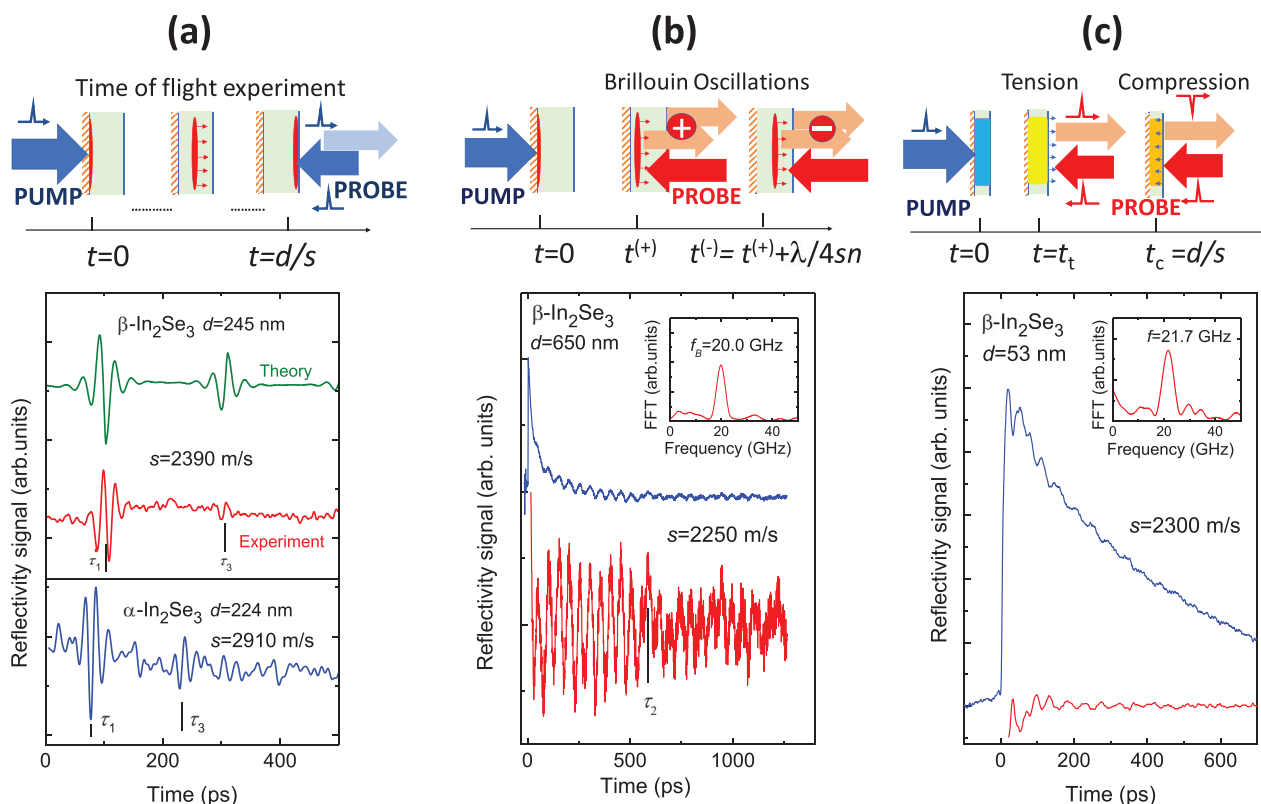
ADVANCED
SCIENCE NEWS
www.advancedsciencenews.com

ADVANCED
FUNCTIONAL
MATERIALS
www.afm-journal.de

Figure 2. Picosecond ultrasonic measurement schemes (upper panels) and typical temporal pump-probe signals (lower panels). Coherent phonons are generated in the flake by an optical pump pulse with $\lambda = 400$ nm from the side of the substrate and detected by probe pulses (400 or 800 nm) at the opposite side of the flake. a) Phonons propagate to the opposite side of the flake, where they are detected with the strongly absorbed 400 nm probe pulse. The spikes in the signal appear at the time when phonons arrive at the flake surface after a single passage across the flake ($t = \tau_1$) or after reflections at the free surface and flake/substrate interface ($t = \tau_3 = 3\ \tau_1$). b) While propagating across the flake, coherent phonons reflect the probe pulse with $\lambda = 800$ nm, which interferes with the probe pulse reflected from the flake surface, resulting in temporal oscillations at the Brillouin frequency. c) The optical pump pulse excites coherent vibrations of the flake, which are detected by the probe optical pulse. Oscillations are due to the first quantized phonon mode for the case of a poor contact at flake/substrate interface. b,c) Signals as-measured (upper, blue) and after background subtraction (lower, red). The insets in (b,c) show the fast Fourier transforms of the signals.

(for details see Experimental section). Pump optical pulses with wavelength $\lambda = 400$ nm from the femtosecond laser excite coherent phonons in the In_2Se_3 flake. These are detected by measuring the reflectivity of the probe laser pulses with $\lambda = 800$ or 400 nm. The principles of the PU technique are described elsewhere[29,30] and the details of the PU experiments applied to other vdW layers can be found in earlier publications.[32–39]

We use three PU methods for extracting the sound velocity s from the temporal dependence of the pump-probe signal. The schematics of these methods are illustrated in the upper panels of **Figure 2**. The choice of the method is governed by the ratio of the optical absorption length x_a and the thickness, d, of the flake. For the pump beam ($\lambda = 400$ nm), we measure $x_a \approx 40$ nm for α-In_2Se_3 and ≈ 30 nm for β-In_2Se_3. These values are in the agreement with earlier optical studies of In_2Se_3.[40] For thick flakes ($d \gg x_a$) coherent phonons excited by the pump in the near-surface region propagate in the form of a strain pulse to the opposite side of the flake where they are detected by the probe pulse. For thin flakes ($d \leq x_a$) the pump excites the whole flake, which results in the generation of resonant breathing phonon modes.[32–38] The sensitivity of the probing method is governed by the photoelastic properties of the mate-

rial and interference of the probe beam on the studied flake. In contrast to vdW materials with a direct bandgap and strong excitonic resonances (e.g., MoS_2,[32] $MoSe_2$[37]), the absorption energy edge for the indirect bandgap In_2Se_3 is broad, which results in a low sensitivity to dynamical strain and in low reflectivity changes induced by a pump pulse.[30] This prevents the detection of coherent phonons in In_2Se_3 flakes with $d < 30$ nm. Three examples of the measured pump-probe signals are shown in the lower panels of Figure 2, each associated with a particular method:

i) Time of flight measurements. This method is very efficient for flakes with $d > 100$ nm. Phonons generated by the pump pulse within the absorption length propagate to the opposite side of the flake where they are probed by optical pulses with $\lambda \approx 400$ nm. Figure 2a shows examples of the measured probe reflectivity signals $R(t)$ and their simulation in β-In_2Se_3 and α-In_2Se_3. The $R(t)$ traces show the distinct responses from coherent phonons arriving at the flake surface after a single (at $t \sim \tau_1$) or triple (at $t \sim \tau_3$) path across the flake. The sound velocity in this case is $s = d/\tau_1$ or $s = 3d/\tau_3$. In all α-In_2Se_3 samples, the phonon-induced signals for a probe have smaller

amplitude than in β-In$_2$Se$_3$ samples. The reason for this is probably their different sensitivities to dynamical strain, which is proportional to the derivative of refractive index, n, on λ.[29,30] Our results suggest that $dn/d\lambda$ in α-In$_2$Se$_3$ is smaller than in β-In$_2$Se$_3$ due to the different electronic band structures.

ii) Brillouin oscillations are detected in flakes with $d > \lambda/n$, where n is the refractive index of the flake. This method is reliable for flakes with $d > 200$ nm. For a probe pulse with $\lambda \approx 800$ nm the flake may be considered as a transparent one,[40] and the probe light being reflected from the propagating phonon wave packet interferes with light reflected from the surface of the flake. As a result, $R(t)$ reveals temporal oscillations as shown in the example of Figure 2b.[41,42] The frequency of these oscillations is $f_B = 2sn/\lambda$. In the flakes with $d > 300$ nm the value of s may be also extracted from the time τ_2 marked in Figure 2 by a vertical line when the oscillation amplitude changes instantly due to the reflection of the phonon wavepacket at the flake/substrate interface. In our experiments coherent phonons are generated by the pump pulse at the interface and thus the first echo arrives there at $\tau_2 = 2\tau_1$ and correspondingly $s = 2d/\tau_2$.

iii) Quantized phonons. In thin flakes ($d < 100$ nm), $R(t)$ shows oscillations due to phonon quantization, as reported for various vdW nanolayers.[32–39] In this case, the fundamental frequency of the flake vibrations is given by $f = s/2d$ or $f = s/4d$ depending on the elastic properties of the interface.[36,38] Then the value of s is obtained from the measurements of f or its higher harmonics. Figure 2c shows an example of the signal for quantized phonons in the case of weak flake/substrate elastic stiffness.

The accuracy of each method for measuring s depends on the flake thickness d and in our experiments is better than $\pm 5\%$. The most precise values for s are obtained from time of flight measurements in relatively thick flakes when the response from phonons propagating from one side of the flake to another is clearly measured. In this case, a fit to the $R(t)$ data by the theoretical curve gives a value of s with an accuracy better than 1%.

We present the PU experiments conducted on 14 and 13 flakes of α-In$_2$Se$_3$ and β-In$_2$Se$_3$, respectively. The values of the sound velocity are summarized in **Figure 3**, where the vertical bars show the number of flakes with the measured sound velocity in the interval between $s - \Delta s$ and $s + \Delta s$. The uncertainty in the value of s in a single flake does not exceed $\Delta s = 50$ m s^{-1}. The comparison of the distributions for α- and β-In$_2$Se$_3$ in Figure 3 obviously points at different sound velocities in different polytypes. We obtain mean sound velocities of $\overline{s} = 3000 \pm 200$ m s^{-1} for α-In$_2$Se$_3$ and $\overline{s} = 2300 \pm 130$ m s^{-1} for β-In$_2$Se$_3$. There is a flake-to-flake variation of s for the sound velocity of the studied α- and β-In$_2$Se$_3$. The most likely reasons for this variation are the uncertainty in the thickness due to the flake tilting (up to 1.5°) and various degrees of elastic stiffness at the flake/substrate interface.[36] We also do not exclude twinning effects in the formation of the layer sequence. We did not find any correlation of the measured s with the PU method used, the flake thickness or the quality of the flakes, as measured from the existence of defects revealed
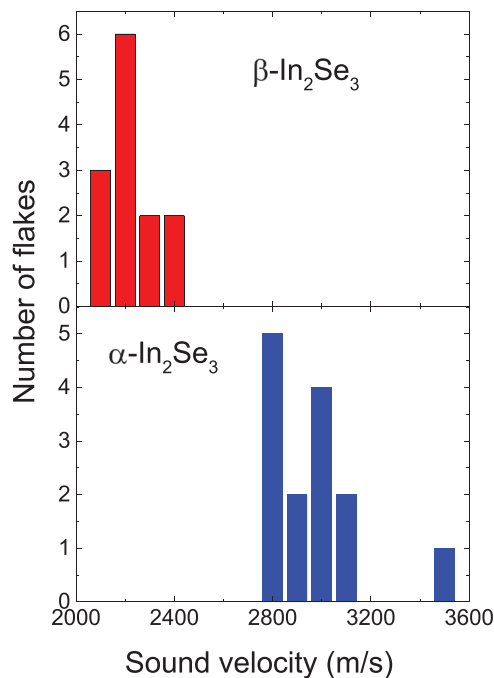

Figure 3. Sound velocity measured by the PU technique in various flakes of α- and β-In$_2$Se$_3$. The height of the bars represents the number of flakes with sound velocity s within an interval $\Delta s = 50$ m s^{-1} centered on s.

by the Raman spectra. Raman spectroscopy was performed on the flakes before and after the pump-probe (PU) measurements to investigate whether the laser induced any modification of the flakes. Some flakes exhibit a slight local amorphization under average pump powers higher than 5 mW. The amorphization of a van der Waals crystal can result into the disappearance of the van der Waals gaps, thus leading to a strong increase of the sound velocity. In our experiments on one α-In$_2$Se$_3$ sample, we observe an increase of velocity of up to 20% relative to the average value. This relatively small increase and the observation of the Raman modes expected for α-In$_2$Se$_3$ suggest only a partial (surface) amorphization of the crystal. For most samples, the change of the sound velocity from the average value is less than 5%, suggesting that the laser-induced damage is minimal and affects mostly the surface of the flake.

The large difference in the sound velocities of α- and β-In$_2$Se$_3$ is the important new finding of this work. The sound velocity in the direction perpendicular to the plane of vdW materials is a characteristic defined by the vdW and intralayer atomic bonding. Experimentally, we measure the net wave elastic modulus $G_\Sigma = c_{33} = s^2 \rho$, where ρ is the density ($\rho_\alpha = 5669$ kg m^{-3}[20] and $\rho_\beta = 5920$ kg m^{-3}[31]). Substituting the measured s, we obtain $G_\Sigma^\alpha = 51 \pm 7$ GPa and $G_\Sigma^\beta = 32 \pm 3$ GPa for α- and β-In$_2$Se$_3$ respectively. As discussed in the following section, the value of G_Σ is directly related to the values of the partial moduli G_g and G_l for the vdW gap and layer, respectively. Thus, to obtain information about the microscopic elastic properties of these very different physical bonds, we performed DFT studies on the vdW and intralayer atomic forces.

2.3. DFT Models and Comparison with the Experiment

In the experiments, the dynamical strain created by the pump excitation has a value of $\approx 10^{-5}$, which corresponds to changes of the total vdW gap and layer thickness by $\approx 10^{-14}$ m. Thus, in the theoretical analysis of elasticity in In_2Se_3 we assume that the deformation created by coherent phonons is small. In this case, we can model the elastic properties of our samples by a series of alternating effective springs, as shown in **Figure 4**. One type of spring with specific stiffness η_l and length x_l models the atomic bonds in the quintuple layer and the other, with stiffness η_g and length x_g, models the vdW bonding between the layers. In this case, one can estimate the net stiffness $\eta_\Sigma = (\frac{1}{\eta_g} + \frac{1}{\eta_l})^{-1}$, the net wave elastic modulus $G_\Sigma = \eta_\Sigma (x_g + x_l)$, and also the partial moduli for the gap, $G_g = \eta_g x_g$, and the layer, $G_l = \eta_l x_l$. To determine $\eta_{l,g}$, we used DFT to calculate the dependence of the total energy of the unit cell E on the variation, x, of either the total thickness of the quintuple layers or the total vdW gap width. Figure 4a,b illustrates the dependences of the relative energy ΔE as the layer thicknesses (upper panels) and vdW gaps (lower panels) are varied for α-In_2Se_3 (2H) and β-In_2Se_3 (3R),

respectively. Here ΔE is the deviation of the energy per unit cell (uc) from its equilibrium value calculated for the unit cell of 10 and 15 atoms for α-In_2Se_3 (2H) and β-In_2Se_3 (3R), respectively. Each unit cell consists of N_L layers which we can represent by N_L springs of stiffness $\eta_{l,g}$ connected in series. Therefore, we estimate $\eta_{l,g} = N_L \ d^2E/dx^2 |_{x=x_0}$, where x_0 is the equilibrium spring length, whose value for different polytypes are given in **Table 1**. The number of layers in the unit cell N_L depends on the polytype: $N_L = 2$ for α-In_2Se_3 (2H) and $N_L = 3$ for β-In_2Se_3 (3R).

The results of the DFT calculations for different In_2Se_3 polytypes are presented in Table 1 together with the net moduli G_Σ obtained from the experiments. In our calculations, we used two different semiempirical methods, D2 and D3, to account for the long-range dispersion contribution to the energy, see Section 4 for details. The calculated equilibrium thicknesses of the layers and gaps are similar to those reported earlier for In_2Se_3.[20,31] Our calculations show that the vdW gaps are much softer than the layers (i.e., $G_l \gg G_g$) in all polytypes, which is consistent with the nature of the different atomic bonds in the layers and gaps. In the former, the forces between atoms are strong due to covalent bonds while the layers are connected with each other by weak vdW forces. Due to essentially softer
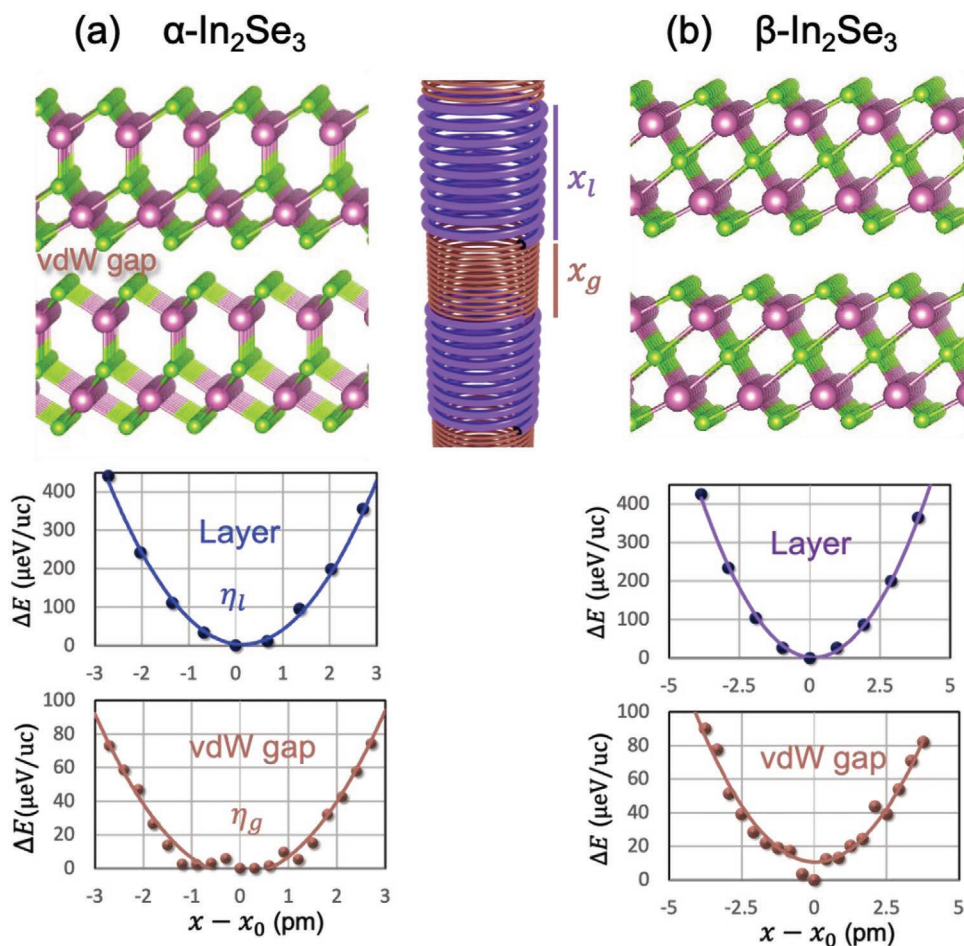

Figure 4. Density functional theory calculations. The schemes of the spring model and the dependences of the unit cell energy on the spring length x for the layers and vdW gaps for a) α-In_2Se_3 (2H) and b) β-In_2Se_3 (3R). $\Delta E = E - E_0$, where E_0 is the equilibrium energy of the unit cell (uc); x_0 is the equilibrium value of the spring length.

Table 1. Elastic parameters calculated by DFT (D2) and DFT (D3) methods for α- and β-In$_2$Se$_3$. The bottom line corresponds to the experimentally measured wave modulus.

DFT method	α-In$_2$Se$_3$				β-In$_2$Se$_3$	
	3R		2H		3R	
	D2	D3	D2	D3	D2	D3
Equilibrium thicknesses (Å)						
Layer, x_l	6.84	6.77	6.85	6.78	6.46	6.43
Gap, x_g	2.83	2.89	2.90	3.01	2.82	2.81
Period, $x_l + x_g$	9.67	9.66	9.75	9.79	9.28	9.24
Specific stiffnesses (10^{19} N m^{-3})						
Layer, η_l	24.4	22.5	23.7	23.1	18.9	18.0
Gap, η_g	7.21	3.88	7.76	4.83	6.87	3.86
Partial modulus (GPa)						
Layer, G_l	167	152	162	157	122	116
Gap, G_g	20.4	11.2	22.5	14.5	19.3	10.8
Net modulus G_Σ, (GPa)						
Theory	54	32	57	39	47	29
Experiment	40.4[a]		51 ± 7		32 ± 3	

[a]The data is taken from the paper by Raranskii et al.[43]

vdW gap over the layer, the net modulus G_Σ is mainly governed by the vdW gap stiffness. However, the role of the final layer stiffness cannot be ignored completely. For instance, for β-In$_2$Se$_3$ (3R), if we assume that the layers are infinitely solid, the calculations with D2 obtain $G_\Sigma = 63$ GPa, which is 30% larger than $G_\Sigma = 47$ GPa calculated for the case which includes the finite stiffness of the layer.

The important result obtained is the pronounced difference in the stiffnesses and the elastic moduli for α-In$_2$Se$_3$ (2H) and β-In$_2$Se$_3$ (3R). The ratios of the elastic moduli calculated using DFT (D3) are $\frac{G_l^\beta}{G_l^\alpha} = 0.74$ for the layers and $\frac{G_g^\beta}{G_g^\alpha} = 0.75$ for the vdW gaps. The difference between layer moduli provides evidence that α-In$_2$Se$_3$ is stiffer than β-In$_2$Se$_3$ due to the different positions of the atoms in the individual layers. On other hand, the ratio of elastic moduli for the vdW gaps suggests that a softer gap is realized for the layer stacking sequence ABCABC in the 3R-polytype compared with the ABAB-stacking in the 2H-polytype. The dependence of the vdW gap modulus G_g on the stacking of neighboring layers points at a possible dependence of the vdW bonding on the thickness of the flake. We note that this dependence is not evident in our experiments on flakes with layer thickness down to about 30 nm. However, it may emerge in the limit of a few atomic layers, which is a prospective task for future experiments and calculations. In contrast, the layer modulus G_l is independent on the stacking, suggesting that it is independent on the layer thickness, as confirmed in our calculations for single α-In$_2$Se$_3$ and β-In$_2$Se$_3$ layers.

From the comparison of the calculated and measured data, we infer that the net modulus G_Σ of α-In$_2$Se$_3$ (2H) is larger than that of β-In$_2$Se$_3$ (3R). The calculated net moduli ratios $\frac{G_\Sigma^\beta}{G_\Sigma^\alpha}$ are equal to 0.77 (DFT-D3) and 0.81(DFT-D2) which compare sat-

isfactory with the measured value of 0.63. However, the absolute value of the calculated parameters of the gap stiffness and modulus strongly depend on the DFT method (D2 or D3). The absolute values of G_Σ are in good agreement with the experiment when calculated by DFT-D2 in α-In$_2$Se$_3$ (2H) and DFT-D3 in β-In$_2$Se$_3$ (3R). This might suggest that the long-range dispersion energy is better approximated by D3 for 3R polytypes and D2 for 2H polytypes. Further investigations of this discrepancy could provide insight into how the dispersion energy should be approximated for crystals with different symmetries.

It is worth mentioning that the sound velocity was also measured by the traditional (MHz) ultrasonic technique in bulk α-In$_2$Se$_3$.[43] In this previous work, the authors obtained $G_\Sigma = 40.4$ GPa, which compares satisfactorily with our theoretical and experimental results. However, we also note that this value is closer to the calculated for α-In$_2$Se$_3$ (3R), which was not available in our PU experiments. This value with its corresponding reference is included in Table 1.

3. Conclusions

In summary, the picosecond ultrasonic probing of the α- and β- polytypes of In$_2$Se$_3$ flakes reveal a significant difference in the sound velocity due to different elastic properties of these materials. The elastic wave modulus of α-In$_2$Se$_3$ (2H) is 60% higher than that of β-In$_2$Se$_3$ (3R). This inequality of the elastic moduli and the corresponding sound velocities is understood by performing DFT calculations using two different models, D2 and D3. The calculation shows that the variation in the net elasticity between two polytypes is the combined result of the atomic bonds in the quintuple layer and the vdW bond. In the extreme case, where the quintuple layer is treated as an infinitely rigid layer, the elastic modulus differs by up to 30%. Therefore, the large reduction of 60% in the elastic modulus of β-In$_2$Se$_3$(3R) compared to α-In$_2$Se$_3$(2H) is governed primarily by the vdW bond in our simple spring model. The comparison of experimental and theoretical results shows that both DFT (D2) and DFT (D3) models sufficiently describe qualitatively the intralayer and vdW bonding and that there is a good quantitative agreement when DFT (D2) and DFT (D3) are applied to α-In$_2$Se$_3$ (2H) and β-In$_2$Se$_3$ (3R), respectively.

Our findings are relevant to the understanding of vdW crystals and their properties, such as emergence and absence of ferroelectricity of the specific polytype α (2H) and β (3R) phases of In$_2$Se$_3$.[26,27] Indeed, the macroscopic polarization in these ferroelectrics and vdW forces are governed by dipole–dipole interactions, and thus they are related to each other. The ultrathin layer regime is particularly interesting for ferroelectric α-In$_2$Se$_3$. The rapid development of epitaxial growth techniques of metal chalcogenides offers a realistic prospect for such studies in the near future. Furthermore, electrons are scattered by phonons whose spectrum is governed by the intralayer and vdW bonding. The efficiency of thermoelectric devices is directly related to the ratio of in-plane and out-of-plane thermal conductivities, which is dependent on the difference of the intralayer and vdW atomic bonding.[44] The significantly different elastic properties of the polytypes suggest that controlled transitions between polytype phases, caused for example by heating and

cooling,[26,27] can be used to tune the acousto-electrical properties of materials like In_2Se_3. Our analysis provides a promising methodology to understand the interlayer forces in vdW crystals that are of fundamental importance for the design and fabrication of heterostructures, including those comprising different types of monolayers and twist angles between the lattices of the layers.

4. Experimental Section

Sample Preparation: Both α-In_2Se_3 (2H) and β-In_2Se_3 (3R) bulk crystals with purity >99.995% were purchased from HQ graphene. Preparation of the flakes follows the same method as in ref. [36]. The crystal structure and phase of the crystals were identified by X-ray diffraction and Raman scattering. The flakes were prepared by mechanical exfoliation using semiconductor grade non-UV dicing tape 6000 series from Loadpoint. Bulk flakes were first exfoliated onto the tape and the exfoliation was repeated two to three times for obtaining higher proportion of thin flakes. The tape with flakes was then immediately brought into contact with a double-side-polished sapphire substrate, which had been freshly washed in acetone followed by an isopropanol rinse. After peeling of the tape, homogenous flakes were identified under an optical microscope. The thickness of the flakes was identified before pump-probe measurement using tapping mode atomic force microscopy under ambient conditions (asylum research MFP-3D). Due to the complex phase diagram of indium selenide and its polytypes, Raman spectroscopy was performed on individual flakes to ensure the phase and quality of the material. The experimental set-up for Raman measurements comprised a He–Ne laser ($\lambda = 633$ nm), an optical confocal microscope system, and a spectrometer with 1200 groves mm equipped with a charge-coupled device. The laser beam was focused to a diameter of about 2 µm using a 100 × objective and the spectra were measured at low power ($P \approx 0.1$ mW) to avoid lattice heating and damage of the flakes.

Picosecond ultrasonic experiments were performed using two Tsunami mode-locked lasers (see Figure 1b) generating pump and probe optical pulses with a duration of 120 fs and repetition rates f_1, $f_2 \approx 80$ MHz. The picosecond temporal resolution between pump and probe pulses was realized by using the asynchronous optical sampling (ASOPS) technique[45] with the offset frequency $\Delta f = f_1 - f_2 = 800$ Hz. The lasers were set on the wavelength ≈800 nm. The pump beam was passed through second harmonic generator (SHG) and optical pulses with wavelength 400 nm were focused on the sample with 30 mm lens from the sapphire substrate side. The pump power did not exceed 10 mW and the diameter of the spot at the sample surface was ≈20 µm. In the time of flight experiments (Figure 2a), the probe beam was passed through another SHG and 400 nm pulses were focused with micro objective 20× at the side of the flake opposite to the pump excitation. The power of the probe beam did not exceed 0.5 mW and the spot diameter was ≈5–7 µm to have the excitation density below the damage threshold. The reflected probe beam is detected by the 10 MHz Newport photodiode (PD), the signals from which were digitized and stored in the computer. Usually, the number of ≈10^5 averages was enough to have a reliable signal for distinguishing the contribution from coherent phonons. Brillouin (Figure 2b) and quantized phonon (Figure 2c) experiments require a large penetration depth for probe beam and we have used 800 nm optical pulses for phonon detection.

The DFT analysis was performed in a plane-wave basis set using the Quantum Espresso code with the Perdew-Burke-Ernzerhof (PBE) generalized gradient approximation.[46,47] To account for the long-range dispersion contribution to the energy, two semiempirical methods were used, D2[48] and D3,[49] proposed by Grimme et al. The calculations were performed using a $12 \times 12 \times 1$ Monkhorst-Pack k-point grid and a kinetic energy cutoff of 48 Ry.

Conflict of Interest

The authors declare no conflict of interest.

Author Contributions

W.Y. prepared the samples, characterized them with AFM and Raman, and performed picosecond ultrasonic measurements together with A.V.A. J.A.P., and M.T.G. performed DFT calculations and analyzed the data together with A.G.B. A.P., and A.J.K. supervised, respectively, the research in the laboratories used for the sample preparation and Raman studies, and picosecond ultrasonic experiments. All authors took part in the discussions and writing the manuscript.

Data Availability Statement

Research data are not shared.

[1] A. K. Geim, I. V. Grigorieva, *Nature* **2013**, *499*, 419.

[2] Y. Liu, N. O. Weiss, X. Duan, H.-C. Cheng, Y. Huang, X. Duan, *Nat. Rev. Mater.* **2016**, *1*, 16042.

[3] Q. Yang, P. Z. Sun, L. Fumagalli, Y. V. Stebunov, S. J. Haigh, Z. W. Zhou, I. V. Grigorieva, F. C. Wang, A. K. Geim, *Nature* **2020**, *588*, 250.

[4] Y. Deng, Y. Yu, M. Z. Shi, Z. Guo, Z. Xu, J. Wang, H. Chen, Y. Zhang, *Science* **2020**, *367*, 895.

[5] J. M. Park, Y. Cao, K. Watanabe, T. Taniguchi, P. J-Herrero, *Nature* **2021**, *590*, 249.

[6] E. Koren, E. Lörtscher, C. Rawlings, A. W. Knoll, U. Duerig, *Science* **2015**, *348*, 679.

[7] Z. Liu, J. Z. Liu, Y. Cheng, Z. Li, L. Wang, Q. Zheng, *Phys. Rev. B* **2012**, *85*, 205418.

[8] W. Wang, S. Dai, X. Li, J. Yang, D. J. Srolovitz, Q. Zheng, *Nat. Commun.* **2015**, *6*, 7853.

[9] X. Li, M. Sun, C. Shan, Q. Chen, X. Wei, *Adv. Mater. Interfaces* **2018**, *5*, 1701246.

[10] N. Iguiñiz, R. Frisenda, R. Bratschitsch, A. Castellanos-Gomez, *Adv. Mater.* **2019**, *31*, 1807150.

**ADVANCED
SCIENCE NEWS**

www.advancedsciencenews.com

**ADVANCED
FUNCTIONAL
MATERIALS**

www.afm-journal.de

[11] E. Mostaani, N. D. Drummond, V. I. Fal'ko, *Phys. Rev. Lett.* **2015**, *115*, 115501.

[12] G. Han, Z.-G. Chen, J. Drennan, J. Zou, *Small* **2014**, *10*, 2747.

[13] N. Balakrishnan, C. R. Staddon, E. F. Smith, J. Stec, D. Gay, G. W. Mudd, O. Makarovsky, Z. R. Kudrynskyi, Z. F. Kovalyuk, L. Eaves, A. Patanè, P. H. Beton, *2D Mater.* **2016**, *3*, 025030.

[14] G. Almeida, S. Dogan, G. Gertoni, C. Giannini, R. Gaspari, S. Perissinotto, R. Krahne, S. Ghosh, L. Manna, *J. Am. Chem. Soc.* **2017**, *139*, 3005.

[15] R. B. Jacobs-Gedrim, M. Shanmugam, N. Jain, C. A. Durcan, M. T. Murphy, T. M. Murray, R. J. Matyi, R. L. Moore, B. Yu, *ACS Nano* **2014**, *8*, 514.

[16] S. Chen, W. Liu, X. Qiao, X. Wan, K. Shehzad, X. Zhang, Y. Xu, X. Fan, *Small* **2017**, *13*, 1604033.

[17] M. Si, A. K. Saha, S. Gao, G. Qiu, J. Qin, Y. Duan, J. Jian, C. Niu, H. Wang, W. Wu, S. K. Gupta, P. D. Ye, *Nat. Electron.* **2019**, *2*, 580.

[18] S. Wan, Y. Li, W. Li, X. Mao, C. Wang, C. Chen, J. Dong, A. Nie, J. Xiang, Z. Liu, W. Zhu, H. Zeng, *Adv. Funct. Mater.* **2019**, *29*, 1808606.

[19] W. Ding, J. Zhu, Z. Wang, Y. Gao, D. Xiao, Y. Gu, Z. Zhang, W. Zhu, *Nat. Commun.* **2017**, *8*, 14956.

[20] F. Xue, X. He, W. Liu, D. Periyanagounder, C. Zhang, M. Chen, C.-H. Lin, L. Luo, E. Yengel, V. Tung, T. D. Anthopoulos, L.-J. Li, J.-H. He, Z. Zhang, *Adv. Funct. Mater.* **2020**, *30*, 2004206.

[21] F. Xue, W. Hu, K.-C. Lee, L.-S. Lu, J. Zhang, H.-L. Tang, A. Han, W.-T. Hsu, S. Tu, W.-H. Chang, C.-H. Lien, J.-H. He, Z. Zhang, L.-J. Li, X. Zhang, *Adv. Funct. Mater.* **2018**, *28*, 1803738.

[22] Y. Zhou, D. Wu, Y. Zhu, Y. Cho, Q. He, X. Yang, K. Herrera, Z. Chu, Y. Han, M. C. Downer, H. Peng, K. Lai, *Nano Lett.* **2017**, *17*, 5508.

[23] C. Cui, W.-J. Hu, X. Yan, C. Addiego, W. Gao, Y. Wang, Z. Wang, L. Li, Y. Cheng, P. Li, X. Zhang, H. N. Alshareef, T. Wu, W. Zhu, X. Pan, L.-J. Li, *Nano Lett.* **2018**, *18*, 1253.

[24] B. Lv, Z. Yan, W. Xue, R. Yang, J. Li, W. Ci, R. Pang, P. Zhou, G. Liu, Z. Liu, W. Zhu, X. Xu, *Mater. Horiz.* **2021**, *8*, 1472.

[25] A. K. Saha, M. Si, P. D. Ye, S. K. Gupta, *Appl. Phys. Lett.* **2020**, *117*, 183504.

[26] X. Tao, Y. Gu, *Nano Lett.* **2013**, *13*, 3501

[27] C. Zheng, L. Yu, L. Zhu, J. L. Collins, D. Kim, Y. Lou, C. Xu, M. Li, Z. Wei, Y. Zhang, M. T. Edmonds, S. Li, J. Seidel, Y. Zhu, J. Z. Liu, W.-X. Tang, M. S. Fuhrer, *Sci. Adv.* **2018**, *4*, eaar7720.

[28] F. Ke, H. Dong, Y. Chen, J. Zhang, C. Liu, J. Zhang, Y. Gan, Y. Han, Z. Chen, C. Gao, J. Wen, W. Yang, X.-J. Chen, V. V. Struzhkin, H.-K. Mao, B. Chen, *Adv. Mater.* **2017**, *29*, 1701983.

[29] O. Matsuda, M. C. Larciprete, R. L. Voti, O. B. Wright, *Ultrasonics* **2015**, *56*, 3.

[30] C. Thomsen, H. T. Grahn, H. J. Maris, J. Tauc, *Phys. Rev. B* **1986**, *34*, 4129.

[31] S. Popović, A. Tonejc, B. Gržeta-Plenković, B. Čelustka, R. Trojko, *J. Appl. Crystallogr.* **1979**, *12*, 416.

[32] S. Ge, X. Liu, X. Qiao, Q. Wang, Z. Xu, J. Qiu, P.-H. Tan, J. Zhao, D. Sun, *Sci. Rep.* **2014**, *4*, 5722.

[33] R. Beardsley, A. V. Akimov, S. Sandeep, Z. R. Kudrynskyi, Z. D. Kovalyuk, A. Patanè, A. J. Kent, *Sci. Rep.* **2016**, *6*, 26970.

[34] T. Y. Jeong, B. M. Jin, S. H. Rhim, L. Debbichi, J. Park, Y. D. Jang, H. R. Lee, D.-H. Chae, D. Lee, Y.-H. Kim, S. Jung, K. J. Yee, *ACS Nano* **2016**, *10*, 5560.

[35] B. He, C. Zhang, W. Zhu, Y. Li, S. Liu, X. Zhu, X. Wu, X. Wang, H. Wen, M. Xiao, *Sci. Rep.* **2016**, *6*, 30487.

[36] J. D. G. Greener, A. V. Akimov, V. Gusev, Z. R. Kudrynskyi, P. H. Beton, Z. D. Kovalyuk, T. Taniguchi, K. Watanabe, A. J. Kent, A. Patanè, *Phys. Rev. B* **2018**, *98*, 075408.

[37] P. Soubelet, A. A. Reynoso, A. Fainstein, K. Nogajewski, M. Potemski, C. Faugeras, A. E. Bruchhausen, *Nanoscale* **2019**, *11*, 10446.

[38] J. D. G. Greener, E. de Lima Savi, A. V. Akimov, S. Raetz, Z. Kudrynskyi, Z. D. Kovalyuk, N. Chigarev, A. Kent, A. Patané, V. Gusev, *ACS Nano* **2019**, *13*, 11530.

[39] F. Vialla, N. Del Fatti, *Nanomaterials* **2020**, *10*, 2543.

[40] H. T. El-Shair, A. E. Bekheet, *J. Phys. D: Appl. Phys.* **1992**, *25*, 1122.

[41] H. Lin, R. Stoner, H. Maris, J. Tauc, *J. Appl. Phys.* **1991**, *69*, 3816.

[42] O. B. Wright, *J. Appl. Phys.* **1992**, *71*, 1617.

[43] N. D. Raranskii, V. N. Balazyuk, Z. D. Kovalyuk, N. I. Mel'nik, V. B. Gevik, *Inorg. Mater.* **2011**, *47*, 1174.

[44] Z.-G. Chen, G. Han, J. Drennan, J. Zou, *Small* **2014**, *10*, 2747.

[45] A. Bartels, R. Cerna, C. Kistner, A. Thoma, F. Hudert, C. Janke, T. Dekorsy, *Rev. Sci. Instrum.* **2007**, *78*, 035107.

[46] P. Giannozzi, S. Baroni, N. Bonini, M. Calandra, R. Car, C. Cavazzoni, D. Ceresoli, G. L. Chiarotti, M. Cococcioni, I. Dabo, A. D. Corso, S. de Gironcoli, S. Fabris, G. Fratesi, R. Gebauer, U. Gerstmann, C. Gougoussis, A. Kokalj, M. Lazzeri, L. Martin-Samos, N. Marzari, F. Mauri, R. Mazzarello, S. Paolini, A. Pasquarello, L. Paulatto, C. Sbraccia, S. Scandolo, G. Sclauzero, A. P. Seitsonen, A. Smogunov, P. Umari, R. M. Wentzcovitch, *J. Phys.: Condens. Matter* **2009**, *21*, 395502.

[47] P. Giannozzi, O. Andreussi, T. Brumme, O. Bunau, M. Buongiorno Nardelli, M. Calandra, R. Car, C. Cavazzoni, D. Ceresoli, M. Cococcioni, N. Colonna, I. Carnimeo, A. Dal Corso, S. de Gironcoli, P. Delugas, R. A. DiStasio, A. Ferretti, A. Floris, G. Fratesi, G. Fugallo, R. Gebauer, U. Gerstmann, F. Giustino, T. Gorni, J. Jia, M. Kawamura, H.-Y. Ko, A. Kokalj, E. Küçükbenli, M. Lazzeri, M. Marsili, N. Marzari, F. Mauri, N. L. Nguyen, H.-V. Nguyen, A. Otero-de-la-Roza, L. Paulatto, S. Poncé, D. Rocca, R. Sabatini, B. Santra, M. Schlipf, A. P. Seitsonen, A. Smogunov, I. Timrov, T. Thonhauser, P. Umari, N. Vast, X. Wu, S. Baroni, *J. Phys.: Condens. Matter* **2017**, *29*, 465901.

[48] S. Grimme, *J. Comput. Chem.* **2006**, *27*, 1787.

[49] S. Grimmea, J. Antony, S. Ehrlich, H. Krieg, *J. Chem. Phys.* **2010**, *132*, 154104.

2106206 (8 of 8)